Hexagonal $YFe_{1-x}Pd_xO_{3-\delta}$: Nonperovskite Host Compounds for Pd^{2+} and Their Catalytic Activity for CO Oxidation

Jun Li,[†] Udayshankar G. Singh,[‡] Thomas D. Schladt,[†] Judith K. Stalick,[§] Susannah L. Scott,*[,‡,||] and Ram Seshadri*[,†,||]

Materials Department and Materials Research Laboratory, University of California, Santa Barbara, California 93106, Department of Chemical Engineering, University of California, Santa Barbara, California 93106, National Institute of Standards and Technology, Gaithersburg, Maryland 20899, and Department of Chemistry and Biochemistry, University of California, Santa Barbara, California 93106

Received June 6, 2008. Revised Manuscript Received August 4, 2008

Metastable $YFeO_3$ with the hexagonal $YAlO_3$ structure was obtained by a sol−gel process at 700 °C, using metal nitrate precursors with pH control and the appropriate citric acid to nitrate ratio. Under similar conditions, $YFe_{1-x}Pd_xO_{3-\delta}$ ($0 < x \leq 0.1$) compositions were also prepared. The substitution of Fe by Pd stabilizes the $YAlO_3$ structure at higher temperatures. The crystal structures of $YFe_{1-x}Pd_xO_{3-\delta}$ ($0 \leq x \leq 0.1$) were refined by Rietveld analysis of X-ray and neutron powder diffraction data. The parent hexagonal $YFeO_3$ ($x = 0$) crystallizes in the space group $P6_3/mmc$ with $a = 3.5099(3)$ Å and $c = 11.759(2)$ Å. The redox-driven mobility of Pd to integrate into the oxide host as ions and to dissociate from it as *fcc*-Pd nanoparticles was monitored by a combination of X-ray diffraction and X-ray photoelectron spectroscopy. Pd nanoparticles in the reduced samples were detected by scanning backscattered electron microscopy and transmission electron microscopy. The Pd^{2+}-containing materials showed significant low-temperature (near 100 °C) catalytic activity for CO oxidation, comparable to that of highly dispersed PdO/Al_2O_3, despite their relatively low surface areas.

Introduction

Since the 1970s, mixed oxides with the perovskite structure have been found to be catalytically active for reactions involving automobile emissions control.[1−3] A recent noteworthy advance was reported in the three-way automotive catalyst $LaFe_{0.57}Co_{0.38}Pd_{0.05}O_3$ developed by Tanaka and co-workers.[4,5] This catalyst was described as "intelligent" due to its ability to regenerate Pd nanoparticles in response to the redox fluctuations that occur in the exhaust gas stream. They showed, by anomalous X-ray diffraction and X-ray absorption fine structure spectroscopy at the Pd K-edge, that Pd ions migrate out of the host matrix as metallic Pd particles under reducing conditions and reenter the perovskite structure, on the *B* site, as ions under oxidizing conditions. This reversible movement of Pd suppresses agglomeration and growth of the Pd nanoparticles and therefore reduces the loss of catalytic surface area caused by sintering. In comparison with Al_2O_3-supported Pd, the intelligent catalyst displays a prolonged lifetime with the same Pd loading, or even with 70% to 90% lower Pd loading. The Co-free perovskite $LaFe_{0.95}Pd_{0.05}O_3$ prepared by the same researchers exhibited similar self-regenerative properties.[6,7]

Using a combination of neutron scattering and X-ray diffraction, density functional electronic structure (DFT) calculations, and X-ray photoelectron spectroscopy, it was recently demonstrated that perovskite $BaCeO_3$ is an excellent host for Pd^{2+} ions.[8] The system $BaCe_{1-x}Pd_xO_{3-\delta}$ with $0.0 < x \leq 0.1$ and $x \sim \delta$ releases *fcc*-Pd when reduced and reincorporates Pd^{2+} when oxidized. The catalytic activity of Pd-substituted $BaCeO_3$ samples for CO oxidation is fairly high at low temperatures, despite low surface areas of only 1 m^2/g.[9] Contrary to general belief that elemental Pd particles are the most catalytically active species, the investigation attributed the catalytic activity mainly to the presence of cationic Pd^{2+} in the host oxide structure. DFT calculations and neutron pair distribution analysis suggest that Pd in $BaCe_{1-x}Pd_xO_{3-\delta}$ adopts d^8 Pd^{2+} in square-planar coordination in the *B* site of the perovskite structure, with an adjacent oxygen vacancy.

* Corresponding authors. E-mail: sscott@engineering.ucsb.edu (S.L.S.); seshadri@mrl.ucsb.edu (R.S.).
[†] Materials Department and Materials Research Laboratory, University of California, Santa Barbara.
[‡] Department of Chemical Engineering, University of California, Santa Barbara.
[§] National Institute of Standards and Technology.
[||] Department of Chemistry and Biochemistry, University of California, Santa Barbara.

(1) Libby, W. F. *Science* **1971**, *171*, 499.
(2) Voorhoeve, R. J. H.; Johnson, D. W., Jr.; Remeika, J. P.; Gallagher, P. K. *Science* **1977**, *195*, 827.
(3) Croat, J. T.; Tibbetts, G. G.; Katz, S. *Science* **1976**, *194*, 318.
(4) Nishihata, Y.; Mizuki, J.; Akao, T.; Tanaka, H.; Uenishi, M.; Kimura, M.; Okamoto, T.; Hamada, N. *Nature* **2002**, *418*, 164.
(5) Tanaka, H. *Catal. Surv. Asia* **2005**, *9*, 63–73.
(6) Tanaka, H.; Tan, I.; Uenishi, M.; Taniguchi, M.; Kimura, M.; Nishihata, Y.; Mizuki, J. *J. Alloys Compd.* **2006**, *408−412*, 1071.
(7) Tanaka, H.; Uenishi, M.; Taniguchi, M.; Tan, I.; Narita, K.; Kimura, M.; Kaneko, K.; Nishihata, Y.; Mizuki, J. *Catal. Today* **2006**, *117*, 321.
(8) Li, J.; Singh, U. G.; Bennett, J. W.; Page, K.; Weaver, J.; Zhang, J. P.; Proffen, T.; Rappe, A. M.; Scott, S. L.; Seshadri, R. *Chem. Mater.* **2007**, *19*, 1418–1426.
(9) Singh, U. G.; Li, J.; Bennett, J. W.; Rappe, A. M.; Seshadri, R.; Scott, S. L. *J. Catal.* **2007**, *249*, 347–356.

10.1021/cm801534a CCC: $40.75
Published on Web 09/25/2008

In the present work, we demonstrate hexagonal $YFeO_3$ as a nonperovskite redox host for catalytic Pd in CO oxidation. $YFeO_3$ crystallizes in either orthorhombic perovskite or hexagonal ($YAlO_3$-type) structures, depending on preparation conditions.[10,11] The stable high temperature phase adopts the orthorhombic perovskite structure[12] in space group *Pnma* (No. 62), as shown by synchrotron X-ray and neutron diffraction studies.[11,13] The metastable low temperature compound with a hexagonal structure has been studied only by X-ray diffraction, and the reported structural data is incomplete.[10] We report the preparation of hexagonal $YFeO_3$ and Pd-containing solid solutions $YFe_{1-x}Pd_xO_{3-\delta}$ at low temperatures using sol−gel processing. Crystallographic data were obtained from X-ray and constant-wavelength neutron diffraction studies. Pd is incorporated into the host structure as ions, extruded as nanoparticles of elemental Pd under reducing conditions, and reabsorbed back into the hexagonal structure as ions when heated in an oxidizing atmosphere. The cycling of Pd in this nonperovskite host is very similar to that previously observed in perovskite-type oxides.

The orthoferrite $YFeO_3$ with a perovskite structure has been widely studied for its magnetic and magneto-optical properties.[14,15] $YFeO_3$-based catalysts, however, have been explored only for the photocatalytic oxidation of organic dyes[16,17] and the selective catalytic reduction of NO_x to N_2 by propene under lean conditions.[18,19] The experiments using hexagonal $YFe_{1-x}Pd_xO_{3-\delta}$ as catalysts for CO oxidation show that despite relatively low surface areas (14−28 m^2/g), the low-temperature activity of $YFe_{1-x}Pd_xO_{3-\delta}$ for CO oxidation resembles that of highly dispersed PdO on Al_2O_3.

Experimental Section

To prepare single-phase hexagonal $YFeO_3$, analytical grade metal nitrates, $Y(NO_3)_3 \cdot 6H_2O$ (Aldrich, ≥99.9%) and $Fe(NO_3)_3 \cdot 9H_2O$ (Aldrich, ≥99.9%) were dissolved in deionized water in a molar ratio of 1:1. The light orange solution was heated to 60 °C with stirring, and then mixed with an aqueous solution of citric acid (Aldrich, 98−102%). The molar ratio of citric acid to metal nitrates was kept constant at 2:1. The solution turned light green after being neutralized (pH = 7.0) with aqueous NH_3. A dark green viscous gel formed upon heating at 60 °C for several hours. The dried gel was fired at 250 °C for 2 h to decompose the nitrates and eliminate the organic components. The resulting dark brown spongelike products were then pulverized and calcined at 700 °C in air for 10 h to obtain red-brown hexagonal $YFeO_3$. To obtain the orthorhombic phase (light orange in color), the amorphous precursor was heated in air at 850 °C for 10 h.

The Pd-substituted materials $YFe_{1-x}Pd_xO_{3-\delta}$ were prepared in a similar fashion. After adding citric acid (citrate/nitrate molar ratio of 2:1), the pH of the solution was adjusted to 2.0 with aqueous NH_3. Stoichiometric amounts of palladium acetate $Pd(CH_3COO)_2$ (Aldrich, ≥99.9%) were dissolved in acetone and added dropwise to the dark green solution with constant stirring at 60 °C until a yellowish-green gel formed. The gel was then fired at 250 °C for 2 h, ground and calcined in air at 750 °C for 10 h to produce the hexagonal $YFe_{1-x}Pd_xO_{3-\delta}$ phases.

Reductions of the $YFe_{1-x}Pd_xO_{3-\delta}$ samples were carried out at 450 °C for 5 h in flowing 5% H_2/95% N_2 with a heating rate of 5 °C/min. Reoxidations of the reduced samples were carried out in flowing oxygen at 500 °C for 10 h at the same heating rate. The gas flow rate was kept constant at 30 cm^3/min for both reactions.

X-ray powder diffraction (XRD) patterns were measured on a Philips XPERT MPD X-ray diffractometer with Cu Kα radiation at room temperature. In-situ X-ray thermodiffraction studies were carried out on a Bruker D8 Advance powder diffractometer fitted with a Braun position sensitive detector and an Anton Paar sample heating stage. The amorphous precursors were heated in air at 10 °C/min, and data were recorded using a step size of 0.0145 °C and a step time of 0.5 s.

Neutron powder diffraction profiles were collected on the 32-counter high resolution diffractometer BT-1 at the Center for Neutron Research at the National Institute of Standards and Technology. A Cu(311) monochromator, yielding a wavelength of 1.5403(1) Å, was employed. Collimation of 15′ of arc was used before the monochromator, 20′ before the sample, and 7′ before the detectors. The samples (≈10 g) were loaded into vanadium containers 15.6 mm in diameter and 50 mm in length. Data were collected at room temperature over a 2θ range of 3° to 167°. X-ray and neutron data were refined using the Rietveld method as implemented in GSAS-EXPGUI[20] software. Bond valence analysis of the neutron structures made use of the Bond Valence Calculator.[21]

X-ray photoelectron spectra (XPS) were obtained on a Kratos Axis Ultra Spectrometer with a monochromatic Al Kα source (E = 1486 eV). Samples were mounted on a stainless steel sample holder using double-sided carbon tabs. The residual pressure inside the analysis chamber was below 1.3×10^{-7} Pa. Survey spectra over wide ranges of binding energy were acquired using an analyzer pass energy of 160 eV, while high resolution spectra were acquired over smaller ranges at 40 eV pass energy. Binding energies were measured with a precision of ±0.2 eV. Quantitative analysis was performed using standard photoionization cross-sections.[22] The C 1s peak from adventitious hydrocarbon, expected at 284.8 eV, was used to correct binding energies for sample charging effects. Two standards were used for XPS analysis: Pd/γ-Al_2O_3 (5.0 wt % Pd, mean particle size 17 nm, Fisher Scientific) and PdO/γ-Al_2O_3 (2.0 wt % Pd loading, mean particle size 7 nm). Peak-fitting of Pd^0 3d doublets was constrained in the ranges 335.6−335.0 eV and 341.0−339.5 eV, and that for Pd^{2+} 3d doublets, in the ranges 338.5−335.0 eV and 343.0−339.5 eV.

The N_2 sorption isotherms were obtained on a Micromeritics TriStar 3000 instrument at liquid N_2 temperature. Prior to each

(10) Yamaguchi, O.; Takemura, H.; Yamashita, M.; Hayashida, A. *J. Electrochem. Soc.* **1991**, *138*, 1492.
(11) Du Boulay, D.; Maslen, E. N.; Streltsov, V. A.; Ishizawa, N. *Acta Crystallogr.* **1995**, *B51*, 921.
(12) Megaw, H. D. *Crystal Structures: A Working Appproach*; Saunders, W. B., Ed.; Philadelphia, PA, 1973.
(13) Sirota, N. N.; Karavai, A. P. *Vestsi Akademii Navuk Belaruskai SSR, Serya Fizika-Matematychnykh Navuk* **1978**, *2*, 74.
(14) Georgiev, D. G.; Krezhov, K. A.; Nietz, V. V. *Solid State Commun.* **1995**, *96*, 535.
(15) Schmool, D. S.; Keller, N.; Guyot, M.; Krishnan, R.; Tessier, M. *J. Appl. Phys.* **1999**, *86*, 5712.
(16) Wu, L.; Yu, J. C.; Zhang, L.; Wang, X.; Li, S. *J. Solid State Chem.* **2004**, *177*, 3666.
(17) Lu, X.; Xie, J.; Shu, H.; Liu, J.; Yin, C.; Lin, J. *Mater. Sci. Eng., B* **2007**, *138*, 289–292.
(18) Lentmaier, J.; Kemmler-Sack, S.; Knell, G.; Kessler, P.; Plies, E. *Mater. Res. Bull.* **1996**, *31*, 1269–1276.
(19) Lentmaier, J.; Kemmler-Sack, S. *Mater. Res. Bull.* **1998**, *33*, 461–473.
(20) (a) Larson, A. C.; Von Dreele, R. B. *General Structure Analysis System (GSAS)*; Report LAUR 86-748, Los Alamos National Laboratory: Los Almos, NM, 1994. (b) Toby, B. H. *J. Appl. Crystallogr.* **2001**, *34*, 210–213.
(21) Hormillosa, C.; Healy, S.; Stephen, T.; Brown, I. D. *Bond Valence Calculator*, version 2.0, 1993; http://ccp14.ac.uk.
(22) Scofield, J. H. *J. Electron Spectrosc. Relat. Phenom.* **1976**, *8*, 129.

measurement, powder samples were degassed by heating at 90 °C for 1 h, then at 200 °C for 3 h under flowing N_2. Surface areas were determined by application of Brunauer−Emmett−Teller (BET) theory.[23] Pore size distributions were calculated using the Barrett−Joyner−Halenda (BJH) method.[24]

Secondary electron field emission scanning electron microscopy (SEM) was performed on a Sirion XL30 microscope. The Pd nanoparticles in reduced samples were examined by SEM in backscattered electron imaging (BEI) mode, on a Sirion XL40 microscope. SEM samples were mounted on aluminum stubs using double-sided conductive carbon tabs. Carbon coating was applied to the insulating samples prior to imaging. Transmission electron microscope (TEM) images and energy dispersive X-ray (EDX) spectra were obtained on a FEI Tecnai G2 Sphera microscope operated at 200 kV and equipped with an Oxford energy dispersive X-ray analysis (EDX) system. TEM samples were ground in isopropanol and spotted on 300 mesh copper grids.

Temperature-programmed (light-off) reactions were carried out in a fixed-bed reactor, consisting of standard glass tubing (30 mm o.d. × 20 cm) wrapped with heating tape and two unheated glass side arms (8 mm o.d. × 30 cm) for gas inlet and outlet. Each catalyst sample (100 ± 5 mg) was pressed into a self-supporting pellet, 16 mm in diameter, and mounted at the center of the reactor. The temperature of the reacting gases was monitored by a thermocouple positioned inside the reactor, close to the catalyst pellet. Prior to each experiment, the catalyst was treated in flowing N_2 (60 cm^3/min) at 350 °C for 3 h to remove adsorbed moisture. The oxidation of CO was studied under steady-state conditions, using a certified gas mixture containing 1000 ppm CO and 10% O_2 in N_2 (Praxair), at a constant flow rate of 50 cm^3/min (measured at room temperature). At each temperature, the sample was allowed to reach steady-state over 3 h, followed by measurement of CO_2 yield. The temperature was then reset for the next measurement. Outlet gases were fed to a gas phase IR cell for online reaction product analysis. FTIR spectra were recorded with a Shimadzu IR Prestige-21 spectrometer, accumulating 32 scans at a resolution of 2 cm^{-1}. The spectrometer sample compartment was purged with dry CO_2-free air from a Balston purge gas generator, and a background spectrum was subtracted from each sample spectrum to remove residual peaks. Quantitative analysis of the IR spectrum of CO_2 was used to construct the light-off profiles.

Results and Discussion

$YFeO_3$ and Pd Substitution. Initial attempts to introduce Pd into the perovskite structure of orthorhombic $YFeO_3$ failed, presumably due to reduction of Pd^{2+} at temperatures above 1000 °C encountered in the solid state synthesis. Low temperature precursor preparation by the sol−gel method was therefore adopted, with the addition of citric acid as a chelating reagent. The carboxylic acid groups in citric acid are believed to chelate the metal ions, ensuring generation of a viscous gel and preventing agglomeration of the subsequent fine ceramic powders after calcination. Reaction conditions were optimized by adjusting the citrate to nitrate ratio, the pH value and the calcination temperature. It was found that gel formation occurred faster at higher pH values. By raising the pH of the reaction solution, complexation of the metal ions by the chelating ligands is favored, due to the deprotonation of the carboxylic acid groups in citric acid. Cross-linking of these metal complexes by water evaporation leads to the formation of a homogeneous gel with uniform metal distribution. Heating the dried gels at 250 °C for 2 h resulted in spongelike powders, which were then ground to yield the dark brown amorphous precursors.

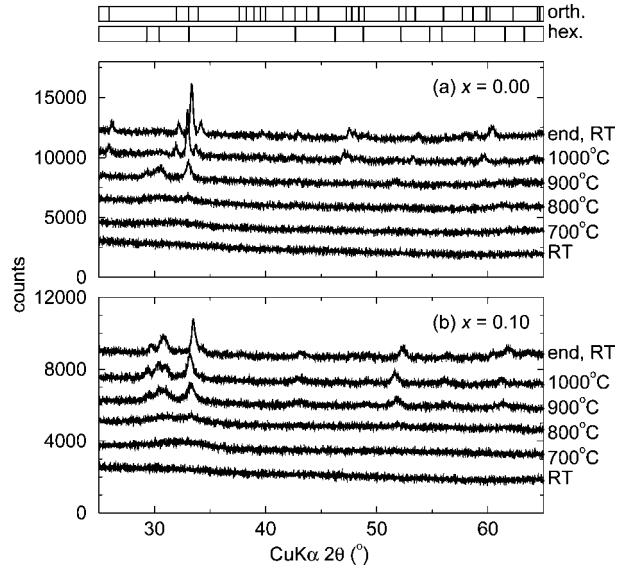

Figure 1. In-situ XRD patterns recorded by heating amorphous precursors of $YFe_{1-x}Pd_xO_{3-\delta}$ in air at 10 °C/min. (a) $x = 0.00$ and (b) $x = 0.10$. Note the stabilization of the hexagonal phase in part b for $x = 0.10$. This phase is only metastable for part a $YFeO_3$. The ending RT data in both panels are shifted significantly in 2θ from the high temperature data due to thermal expansion of the sample. Individual patterns have been vertically offset for clarity. Vertical bars at the top of the figure are the expected peak positions for orthorhombic and hexagonal $YFeO_3$.

In-situ X-ray thermodiffraction was employed to monitor the reaction process (Figure 1). For two precursors, one with 10% Pd substitution [Figure 1b] and one without [Figure 1a], X-ray powder patterns were recorded every 15 min while heating each precursor in air at a constant heating rate under the same conditions. Figure 1a shows that the metastable Pd-free hexagonal phase formed at 900 °C was transformed to the orthorhombic phase at 1000 °C and remained orthorhombic when cooled to room temperature. Figure 1b shows that the Pd-containing hexagonal phase formed at the same temperature and remained in the same structure throughout the entire process. Pd substitution is inferred to stabilize the hexagonal structure. For bulk sample preparation, we obtained single-phase hexagonal $YFeO_3$ at 700 °C and orthorhombic $YFeO_3$ at 850 °C by adjusting the pH of the solution to 7.0 with a citrate to nitrate ratio of 2:1. It has been reported that both pure phases can be synthesized by self-propagating combustion using glycine as a fuel.[16] The combustion flame temperature is as high as 1320 °C in the case of hexagonal $YFeO_3$.

Phase-pure hexagonal $YFe_{1-x}Pd_xO_{3-\delta}$ with $x = 0.00$, 0.05, and 0.10 was prepared in 0.3−0.4 g batches by calcination of the appropriate precursors at 700 °C ($x = 0.00$ only) and 750 °C for 10 h in air. The red-brown color darkened with increasing Pd-substitution. Larger, approximately 2 g batches were prepared nearly phase-pure under the same conditions and combined to produce around 10 g for the constant wavelength neutron study. Diffraction data with single-phase

(23) Brunauer, S.; Emmett, P. H.; Teller, E. *J. Am. Chem. Soc.* **1938**, *60*, 309.
(24) Barrett, E. P.; Joyner, L. G.; Halenda, P. P. *J. Am. Chem. Soc.* **1951**, *73*, 373380.

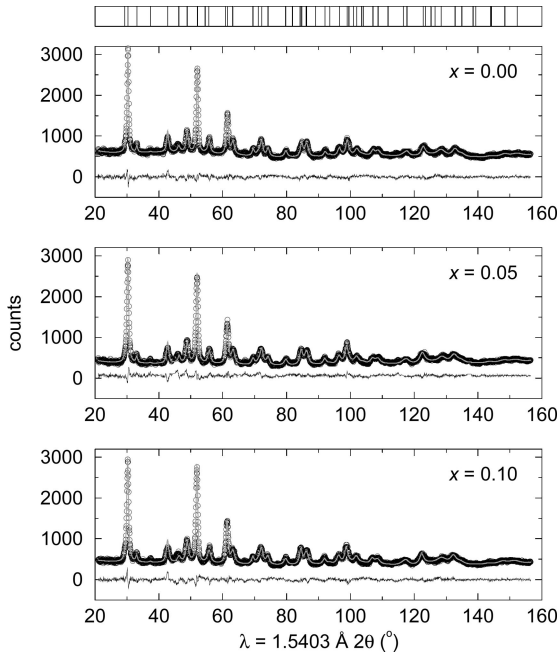

Figure 2. Constant wavelength neutron diffraction Rietveld refinement of $YFe_{1-x}Pd_xO_{3-\delta}$ ($x = 0.00$, 0.05, 0.10). Circles are data, and the gray line is the Rietveld fit. Difference profiles are also shown. Vertical bars at the top of the figure are the expected peak positions for hexagonal $YFeO_3$.

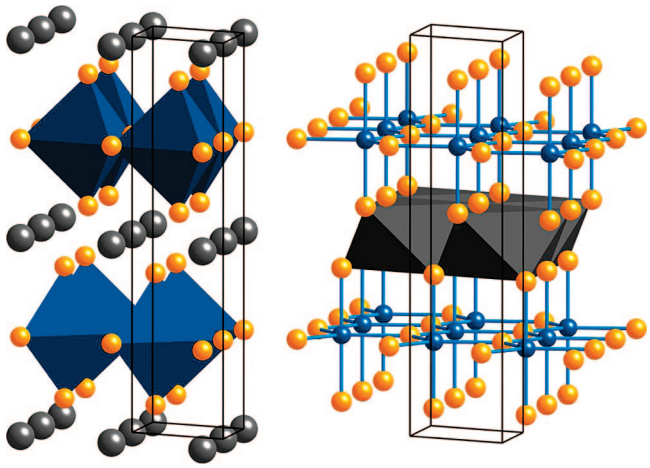

Figure 3. Two different depictions of the crystal structure of hexagonal $YFeO_3$. The gray spheres are Y, small orange spheres are O, and blue spheres are Fe. (a) FeO_5 trigonal bipyramids displayed in blue. (b) YO_6 octahedra depicted in gray.

Rietveld fits are displayed in Figure 2. Some evidence for unreacted Y_2O_3 was seen in the diffraction data, but adding a second phase did not significantly affect the overall fit. The crystal structure of hexagonal $YFeO_3$ is similar to that of hexagonal $YAlO_3$. It consists of alternating layers of corner-sharing FeO_5 trigonal bipyramids and planes of Y [Figure 3a]. Each Y atom can be described as sitting at the center of an edge-sharing octahedron formed by close-packed oxygens, with two additional face-capping oxygens, at longer distances, above and below the octahedron along the *c* axis [Figure 3b]. Crystallographic data are summarized in Tables 1 and 2. The cell volume of $YFe_{1-x}Pd_xO_{3-\delta}$ expands by 0.23% when $x = 0.10$ in the starting composition. The refined stoichiometry of Pd is actually $x = 0.08(2)$ at this composition. Evidence of oxygen vacancies were found in all samples

Table 1. Results of Rietveld Refinement of CW Neutron Diffraction Data on $YFe_{1-x}Pd_xO_{3-\delta}$ Powders[a]

parameters	$x = 0.00$	$x = 0.05$	$x = 0.10$
R_p (%)	3.52	4.79	4.53
wR_p (%)	4.33	5.97	5.73
χ^2	1.28	1.88	1.83
a (Å)	3.5099(3)	3.5145(3)	3.5172(3)
c (Å)	11.759(2)	11.738(2)	11.738(2)
V (Å^3)	125.46(3)	125.57(3)	125.75(3)
O2, *z*	0.0835(3)	0.0830(3)	0.0830(3)
Y, U_{11}	0.009(1)	0.009(1)	0.010(1)
Y, U_{33}	0.036(3)	0.029(3)	0.032(3)
Fe(Pd), U_{11}	0.0101(8)	0.0098(8)	0.0105(7)
Fe(Pd), U_{33}	0.004(2)	0.005(2)	0.006(2)
O1, U_{11}	0.017(2)	0.023(2)	0.023(2)
O1, U_{33}	0.053(4)	0.035(4)	0.038(4)
O2, U_{11}	0.010(1)	0.009(1)	0.010(1)
O2, U_{33}	0.037(3)	0.038(3)	0.037(3)
Pd, occ.		0.04(2)	0.08(2)
BVS(Y)	3.36	3.37	3.37
BVS(Fe)	2.62	2.61	2.60
BVS(Pd)		2.02	2.02
BVS(O1)	1.62	1.61	1.61
BVS(O2)	2.18	2.18	2.18

[a] Note: The crystal structure is described in space group $P6_3/mmc$ (No. 194) with Y at 0, 0, 0; Fe, Pd at $^1/_3$, $^2/_3$, $^1/_4$; O1 at 0, 0, $^1/_4$; O2 at $^1/_3$, $^2/_3$, *z*. O1 and O2 are at the equatorial and axial positions, respectively, of the FeO_5 trigonal bipyramid. Anisotropic temperature factors (Å^2) are expressed as: $\exp[-2\pi^2 \times (U_{11}h^2a^{*2} + U_{22}k^2b^{*2} + U_{33}l^2c^{*2} + 2U_{12}hka^*b^* + 2U_{13}hla^*c^* + 2U_{23}klb^*c^*)]$, and $U_{11} = U_{22} = 2U_{12}$, $U_{13} = U_{23} = 0$. Standard uncertainties, given in parentheses, do not reflect the undertainty in the neutron wavelength. Bond valence sums (BVS) were calculated using the Bond Valence Calculator.[21]

Table 2. Bond Distances (Å) and Bond Angles (deg) in $YFe_{1-x}Pd_xO_{3-\delta}$

	$x = 0.00$	$x = 0.05$	$x = 0.10$
Y−O1, ×2	2.9397(4)	2.9346(5)	2.9345(5)
Y−O2, ×6	2.252(1)	2.251(1)	2.251(1)
Fe−O1, ×3	2.0265(1)	2.0291(2)	2.0307(2)
Fe−O2, ×2	1.958(3)	1.960(3)	1.960(3)
O2−Y−O2	102.40(9)	102.64(8)	102.66(8)
Y−O2−Y	102.40(9)	102.64(8)	102.66(8)
Y−O2−Fe	115.86(7)	115.65(7)	115.64(7)

regardless of Pd substitution, but the refinements were never sufficiently stable for quantitative analysis. On the basis of bond valence calculations, Fe is underbonded compared with Y in this structure. No antisite defects were found which could account for this. In hexagonal $YAlO_3$ and $YMnO_3$ (high temperature phase) with space group $P6_3/mmc$, Al and Mn are also highly underbonded in the center of trigonal bipyramids of oxygens.[25,26] The bond valence of Pd, although calculated from the average structural model, is very close to 2. The previous study on Pd-substituted $BaCeO_3$ showed that the propensity of d^8 Pd^{2+} to adopt square-planar coordination is satisfied by a combination of oxygen vacancy formation and through tilting of the adjacent CeO_5 square pyramid.[8] No evidence for such a mechanism is found in the present set of compounds, and it is difficult to envisage the formation of square planes in the *B* site of the $YAlO_3$ structure. However, Pd^{2+} ions readily adopt trigonal bipyramidal coordination, as required in the *B* site of the hexagonal structures found here. In fact, 5-coordination exists

(25) Bertaut, F.; Mareschal, J. *Fr. Compt. Rend.* **1963**, *257*, 867.
(26) Lukaszewicz, K.; Karut-Kalicinska, J. *Ferroelectrics* **1974**, *7*, 81.

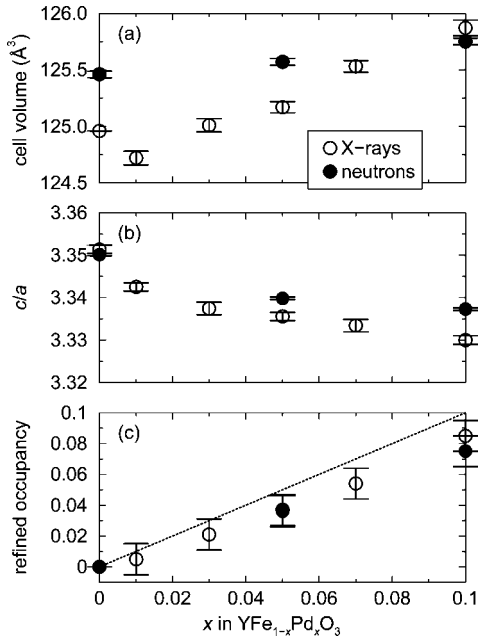

Figure 4. Impact of Pd substitution on (a) the cell volume and (b) the *c*/*a* ratio of hexagonal $YFe_{1-x}Pd_xO_{3-\delta}$, as obtained from Rietveld refinement. Panel c displays the refined amount of Pd on the Fe site, as a function of the nominal amount *x*. The dashed line in panel c shows the intended substitution level. Error bars correspond to 1 σ.

widely in d^8 metal complexes.[27,28] Local structure probes of Pd coordination such as EXAFS are required to confirm this issue. The preference of Pd^{2+} for 5-coordination (trigonal bipyramids) over 6-coordination (octahedra) would help to explain why Pd-substitution in $YFeO_3$ stabilizes the hexagonal structure and avoids conversion to the perovskite.

The crystal structure of $YFeO_3$ was also refined using, as a model, hexagonal polar $YMnO_3$ (low temperature phase) with space group $P6_3cm$. This improved the fit only slightly at the expense of many more parameters and resulted in unstable refinement of thermal parameters. The bond valence of Fe is near 2.6 in both structure types, but that of Y drops from 3.3 to 2.8 by allowing tilting of the FeO_5 pyramids upon lowering the symmetry. The structure reported here is the $P6_3/mmc$ $YAlO_3$ type, but other possible structures require exploration.

A series of $YFe_{1-x}Pd_xO_{3-\delta}$ samples with Pd substitution between $x = 0.00$ and 0.15 were prepared by a similar method, in approximately 0.35 g batches. These materials were characterized using Rietveld refinement of powder X-ray diffraction data. Compositions of $YFe_{1-x}Pd_xO_{3-\delta}$ ($0 \leq x \leq 0.1$) were verified to be nearly single phase, with the amount of Pd on Fe site refined to be close to 0.08(2) for the $x = 0.10$ sample. The average crystallite size of $YFe_{1-x}Pd_xO_{3-\delta}$ is around 20 nm, as determined by Scherrer line broadening analysis of the X-ray diffraction patterns. Impurity phases such as Y_2O_3 and PdO were detected in samples with Pd substitution levels higher than $x = 0.10$. The evolution of the $YFe_{1-x}Pd_xO_{3-\delta}$ structures with *x*, as obtained from neutron and X-ray diffraction data, is shown in Figure 4. The expansion of cell edge *a* and contraction of cell edge *c* upon substitution result in increasing cell volume and decreasing axial *c*/*a* ratio. The deviation of the cell volume of the undoped sample ($x = 0.0$) from the trend is perhaps due to its lower preparation temperature. The discrepancies between neutron and X-ray diffraction results for the refined lattice parameters may be caused by a number of experimental factors, including sample position, treatment of profile line shapes, variability in batch preparation of samples, and the sample volume irradiated. The *c*/*a* ratio, on the other hand, is much less influenced by variability across experiments, so that clearer trends and better neutron/X-ray agreement are seen. On the basis of neutron analysis (Table 2), with increasing *x*, the elongated distances between Fe and its three equatorial oxygens (O1) seem to account for the change in cell edge *a*, while the change in cell edge *c* is a consequence of YO_6 octahedral layer getting thinner along the *c* axis, as reflected by the relatively rigid Y−O2 bond and increasing O2−Y−O2 and Y−O2−Y bond angles with *x*. The change in bond angles also shortens the distances between Y and the equatorial oxygens (O1) (Table 2). The cell volume expansion can be attributed to the replacement by the larger Pd^{2+} ions of the smaller Fe^{3+} ions.

Redox Cycles: Bulk and Surface Characterization. A series of reduction and reoxidation treatments were performed on an as-prepared sample of $YFe_{1-x}Pd_xO_{3-\delta}$ ($x = 0.10$), to examine the mobility of Pd in the bulk material. In flowing 5% H_2/95% N_2, the hexagonal host extruded elemental *fcc*-Pd when heated above 200 °C and decomposed completely to Y_2O_3, elemental Fe, and Pd above 600 °C. Subsequent reductions were conducted exclusively at 450 °C so as to avoid such complete decomposition. The released elemental Pd, together with Y_2O_3, were reabsorbed into the host lattice upon reoxidation at 500 °C for 10 h in pure O_2. The bulk structure is expected to transform completely from hexagonal to orthorhombic if the reoxidation is conducted above 700 °C. All reoxidation experiments were carried out at 500 °C in order to retain the hexagonal structure. The reversible movement of Pd was verified through repeated redox cycling. Figure 5a shows XRD patterns and corresponding one- or two-phase Rietveld fits for a $YFe_{1-x}Pd_xO_{3-\delta}$ ($x = 0.10$) sample through two redox cycles. Starting with the as-prepared, single phase sample, we observe the appearance of the (111) reflection of *fcc*-Pd near 41° 2θ upon reduction. This peak disappears upon reoxidation. The very small crystallite size of the extruded Pd results in the peak being broad and weak. The average crystallite size of the elemental Pd was calculated to be 12 nm by two-phase Rietveld analysis. The hexagonal structure is maintained upon reduction and subsequent reoxidation around 500 °C. The mole fraction of elemental Pd was found to be $6 \pm 0.3\%$ in the reduced samples by two-phase Rietveld analysis [Figure 5b], and single-phase $YFe_{1-x}Pd_xO_{3-\delta}$ ($x = 0.10$) was essentially recovered after reoxidation. The calculated cell volume as a function of redox treatment is shown in Figure 5c. Interestingly, the extrusion of Pd results in an expansion of the host lattice, instead of the shrinkage expected from Pd^{2+} being larger than Fe^{3+}. This unexpected cell volume increase is attributed to the loss of lattice oxygen upon reduction.

(27) Auf der Heyde, T. P. E.; Burgi, H.-B. *Inorg. Chem.* **1989**, *28*, 3960.
(28) Morgan, T. D. B.; Tobe, M. L. *Inorg. Chim. Acta* **1971**, *5*, 563.

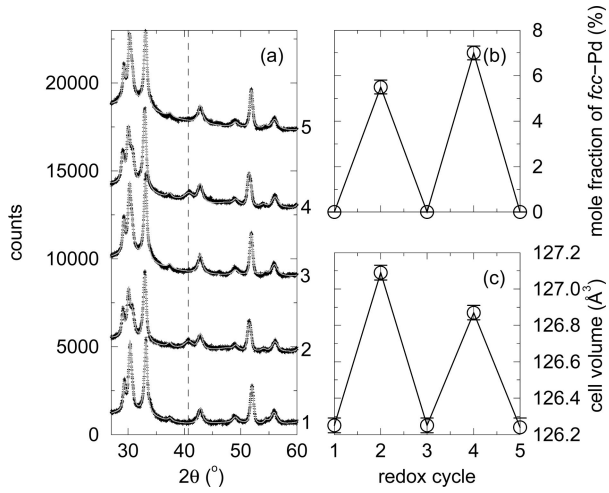

Figure 5. Cycling of Pd into and out of the hexagonal host, driven by redox. (a) Observed (crosses) and calculated (gray lines) XRD data of an as-prepared $YFe_{1-x}Pd_xO_{3-\delta}$ ($x = 0.10$) sample (1), subjected alternately to reduction (2,4) at 450 °C for 5 h in 5% H_2/95% N_2 and oxidation (3,5) at 500 °C for 10 h in pure O_2. The dashed line indicates the position of the (111) reflection of *fcc*-Pd. The data and fits are verically offset but plotted on the same vertical scale in order to compare intensities. (b) Amount of elemental Pd, in mole fraction percent. (c) Change in cell volume in response to the redox variation. The lines in parts b and c are drawn to guide the eye. Error bars correspond to 1σ.

Also noted in Figure 5a is that the diffraction peak near 52° 2θ shifts to lower angle upon reduction and reverts to its original position upon reoxidation. An opposite shift occurs for the peak near 31° 2θ. These are the (110) and (004) reflections of hexagonal $YFeO_3$, respectively. Appreciable shifting of these two peaks indicates significant expansion in the *ab* plane and contraction along the *c* axis upon reduction. If the lost oxygens are the equatorial oxygens of FeO_5 trigonal bipyramids in the hexagonal structure (Figure 3), increased cation−cation repulsion between Fe^{3+} in the *ab* plane, and decreased anion−anion repulsion along the *c* axis would account for the anisotropic change in cell edges, i.e., the cell *a* parameter expands by 0.76%, while the cell *c* parameter contracts by 0.85%.

The reduction of Pd^{2+} and its regeneration upon reoxidation were also examined by high resolution X-ray photoelectron spectroscopy in the Pd 3d region (Figure 6). The signals for the Pd 3d levels are deconvoluted into pairs of spin−orbit doublets: $3d_{5/2}$ and $3d_{3/2}$. The peaks at 337.3 and 342.7 eV in the spectrum of as-prepared $YFe_{1-x}Pd_xO_{3-\delta}$ ($x = 0.10$) are assigned to Pd^{2+} present in the hexagonal host. The binding energies of these peaks are blue-shifted by approximately 0.7 eV with respect to the peak positions of 336.7 and 342.0 eV found for Pd $^{2+}$ in the PdO standard. This shift could be caused by a more ionic environment for the Pd ions incorporated in the trigonal bipyramidal sites of the hexagonal structure than in the square pyramidal sites of PdO. A shift of 1.0 eV to higher binding energy was observed for Pd $^{2+}$ in the highly ionic *B* site of perovskite $BaCe_{1-x}Pd_xO_3$.[8] Upon reduction at 450 °C for 5 h in 5% H_2/95% N_2, two new peaks for Pd^0 appear at 335.6 and 340.8 eV. These positions are consistent with the binding energies 335.4 and 340.5 eV obtained for the Pd^0 standard. The intensity of the Pd^0 signals was not attenuated as it was in reduced $BaCe_{1-x}Pd_xO_3$, where it was attributed to overgrowth

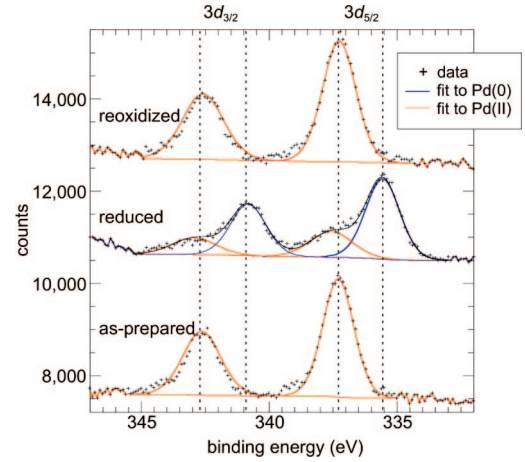

Figure 6. High-resolution XPS scans of $YFe_{1-x}Pd_xO_{3-\delta}$ ($x = 0.10$) in the Pd 3d region. Spectra are verically offset but plotted on the same vertical scale in order to compare intensities.

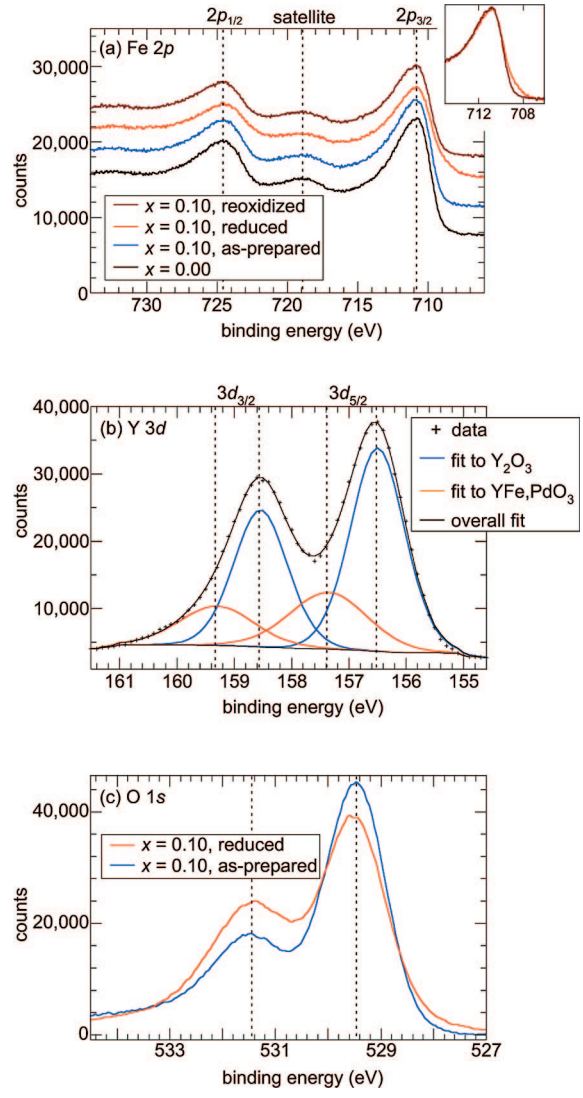

Figure 7. High-resolution XPS scans of $YFe_{1-x}Pd_xO_{3-\delta}$. (a) Fe 2p region. (b) Y 3d region. (c) O 1s region. Spectra in part a are verically offset but plotted on the same vertical scale in order to compare intensities.

of the perovskite.[8] The persistence of a small amount of Pd^{2+} is presumably due to incomplete reduction under the mild conditions employed in the reaction. Exposing the sample

Table 3. Surface Atomic Ratios in Hexagonal $YFe_{1-x}Pd_xO_{3-\delta}$[a]

samples	treatment	Y 3d	Fe 2p	Pd 3d	O 1s	Y/(Fe + Pd)
$x = 0.00$	as-prepared, precatalysis	27.5	8.2	0.0	64.3	3.3
$x = 0.10$	as-prepared, precatalysis	27.9	7.8	1.5	62.8	3.0
	as-prepared, postcatalysis	29.3	7.4	1.5	61.8	3.3
	reduced, precatalysis	26.8	6.1	1.3	65.8	3.6
	reduced, postcatalysis	30.9	5.7	1.3	62.1	4.4
	reoxidized, precatalysis	25.3	7.0	1.5	66.2	3.0
	reoxidized, postcatalysis	30.3	6.6	1.4	61.7	3.8
$x = 0.05$	as-prepared, precatalysis	28.9	7.4	1.0	62.8	3.5
	as-prepared, postcatalysis	30.3	6.9	1.1	61.7	3.8
	reduced, precatalysis	27.6	6.5	0.8	65.2	3.8
	reoxidized, precatalysis	25.3	6.8	1.0	67.0	3.3
	reoxidized, postcatalysis	29.7	6.4	1.1	62.8	4.0

[a] Surface compositions are uncorrected for differing escape depths of photoelectrons from different elements.

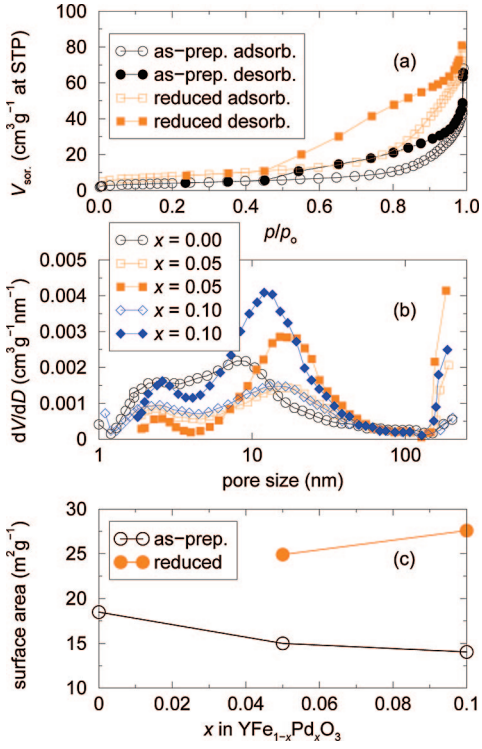

Figure 8. (a) N_2 sorption isotherms at 77 K for $YFe_{1-x}Pd_xO_{3-\delta}$ with $x = 0.10$. (b) BJH pore size distributions for different samples of $YFe_{1-x}Pd_xO_{3-\delta}$ whose x values are indicated in the figure. Open symbols refer to the as-prepared samples and filled symbols to the samples after reduction. (c) BET surface areas obtained for the different samples.

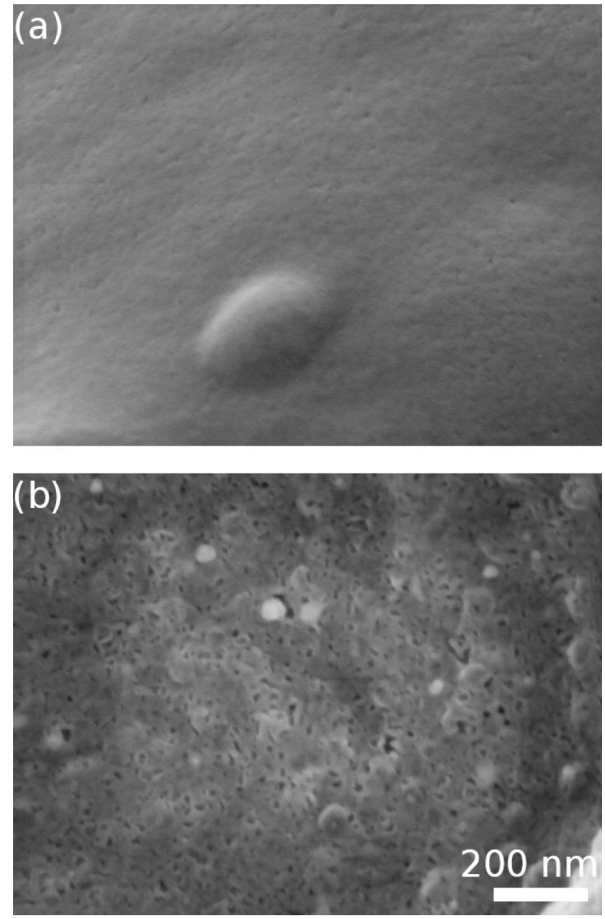

Figure 9. SEM images of as-prepared (a) and reduced (b) samples of $YFe_{1-x}Pd_xO_{3-\delta}$ ($x = 0.10$). Roughening of the monolith surface and the development of some porosity in part b is noted. The scale bar is common to both panels.

to air immediately after reduction and transferring it to the XPS chamber in air could also cause partial oxidation of Pd^0 on the surface. Signals from Pd^{2+} were totally recovered, and those of Pd^0 completely disappeared, upon heating the reduced sample at 500 °C for 10 h in pure O_2. Similar changes were seen for samples of $YFe_{1-x}Pd_xO_{3-\delta}$ ($x = 0.05$).

Analysis of Surface Composition by XPS. For $YFe_{1-x}Pd_xO_{3-\delta}$ ($x = 0.10$), the Fe $2p_{1/2}$ and $2p_{3/2}$ signals were located at 724.5 and 710.9 eV, respectively, in the Fe 2p spectra [Figure 7a], regardless of Pd substitution. These values are consistent with Fe^{3+} in Fe_2O_3 and in hexagonal $YFeO_3$, as is the presence of the core-level satellite at 718.8 eV.[16,29] The superimposed spectra show shoulders on the low energy side of each peak in the spectrum of reduced $YFe_{1-x}Pd_xO_{3-\delta}$ ($x = 0.10$), exemplified by Fe $2p_{3/2}$ peak in the inset of Figure 7a. These new lines are attributed to a small amount of Fe^{2+} in the hexagonal structure, formed upon loss of lattice oxygen during reduction. The peak position of Fe^{2+} $2p_{3/2}$ is close to that found for spinel Fe_3O_4, which contains a mixture of Fe^{3+} and Fe^{2+}.[30] These reduction-induced features disappeared when the sample was reoxidized. This is experimental confirmation of the existence of oxygen vacancies in reduced $YFe_{1-x}Pd_xO_{3-\delta}$, consistent with the lattice expansion observed by XRD.

(29) Wagner, C. D.; Riggs, W. M.; Davis, L. E.; Moulder, J. F.; Muilenberg, G. E. *Handbook of X-ray Photoelectron Spectroscopy*; Physical Electronics Division, Perkin-Elmer Corp.: Eden Prairie, MN, 1979.

(30) McIntyre, N. S.; Zetaruk, D. G. *Anal. Chem.* **1977**, *49*, 1521.

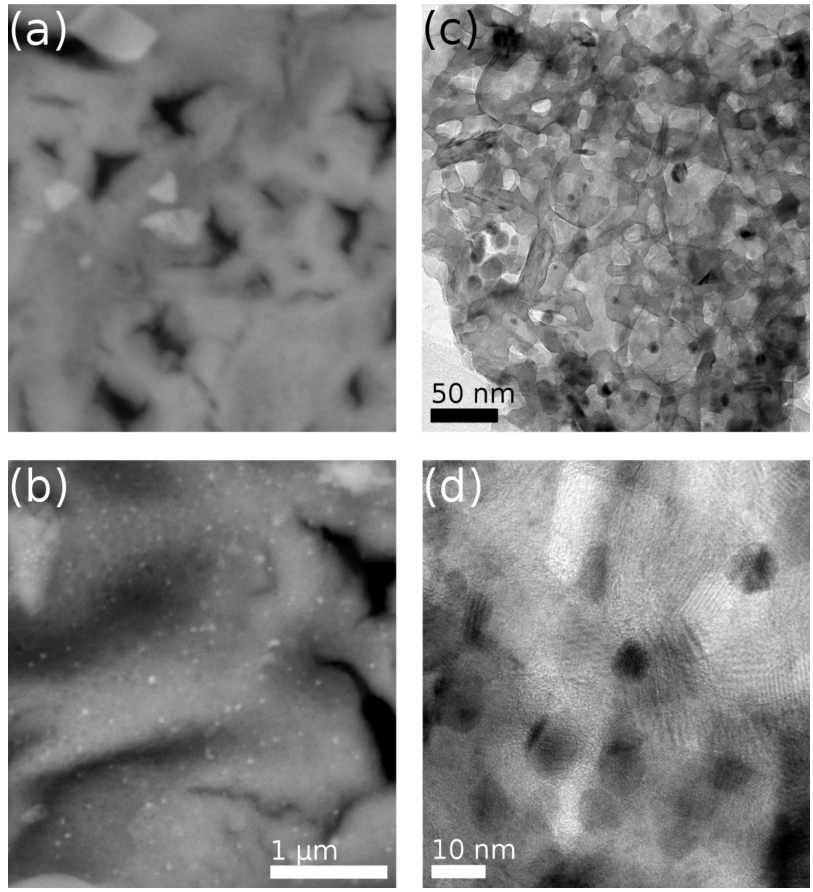

Figure 10. (a) Backscattered electron image of as-prepared $YFe_{1-x}Pd_xO_{3-\delta}$ ($x = 0.10$). (b) Same sample after reduction, at the same magnification, showing Pd nanoparticles observed as light spots in the backscattered electron image. (c and d) Transmission electron microscope images of the reduced $YFe_{1-x}Pd_xO_{3-\delta}$ ($x = 0.10$) sample acquired at two different magnifications. The *fcc*-Pd nanoparticles appear as dark, roughly 10 nm-sized spheres.

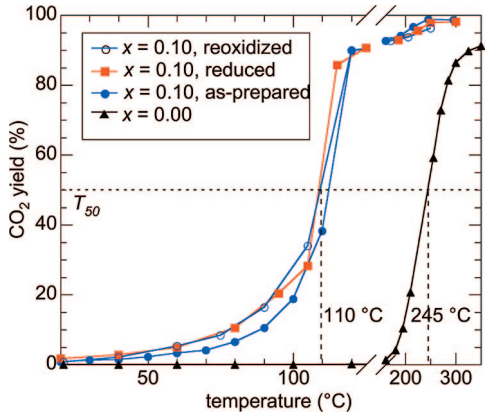

Figure 11. Temperature-programmed reaction profiles for the oxidation of CO (1000 ppm) by excess O_2 (10% in N_2, total flow rate 50 cm^3/min) over 100 mg $YFe_{1-x}Pd_xO_{3-\delta}$ ($x = 0.00, 0.10$). Lines are drawn as guides to the eye.

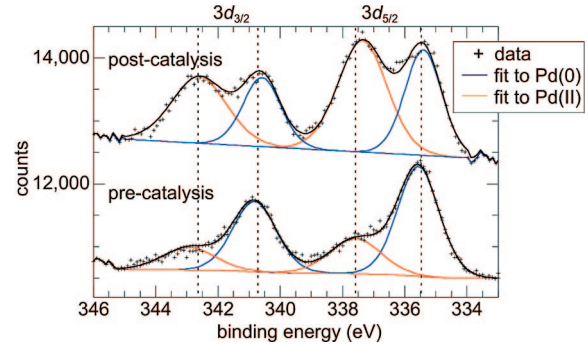

Figure 12. XPS spectra of reduced $YFe_{1-x}Pd_xO_{3-\delta}$ ($x = 0.10$) in Pd 3d region, before and after catalysis of CO oxidation in an O_2-rich atmosphere. Spectra are verically offset but plotted on the same vertical scale in order to compare intensities.

Two spin−orbit doublets were resolved by spectral deconvolution in the high resolution scan of the Y 3d region [Figure 7b], with a major doublet at 158.5 and 156.5 eV and a minor doublet at 159.4 and 157.4 eV. No difference was observed in the spectra of samples with different Pd contents, including $x = 0$. The Y $3d_{5/2}$ peak position at 156.5 eV is in good agreement with 156.6 eV reported for Y_2O_3.[29] Given its high surface free energy, the ca. 1% Y_2O_3 impurity seems to be preferentially found on the surface, where it is the major contributor to the signals in the Y 3d region. The pair of peaks at higher binding energies ($3d_{5/2}$ at 157.4 eV) are attributed to subsurface $YFeO_3$. The shift in binding energy indicates a more ionic Y−O bonding in $YFe_{1-x}Pd_xO_{3-\delta}$ than in Y_2O_3, consistent with the bond valence calculation of neutron analysis. In the hexagonal structure of $YFe_{1-x}Pd_xO_{3-\delta}$, Y is overbonded with a bond valence sum of 3.36 to 3.37 (Table 1). The Y_2O_3 thin overlayer causes the surface to be enriched in Y and depleted in Fe for all samples (Table 3). The total Pd content at the surface, calculated from the survey scan, is close to its bulk concentration, indicating that the Pd dispersion is nonuniform, with a Pd-enriched surface. Although the oxidation

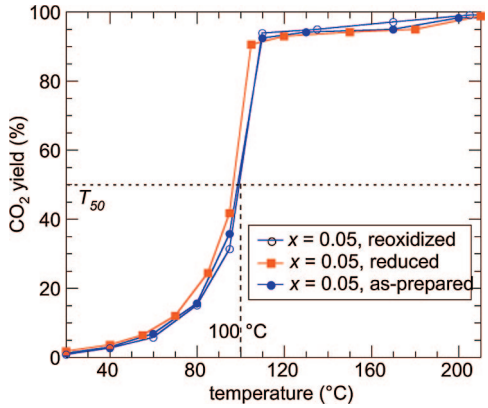

Figure 13. Temperature-programmed reaction profiles for the oxidation of CO (1000 ppm) by excess O_2 (10% in N_2, total flow rate 50 cm^3/min) over 100 mg $YFe_{1-x}Pd_xO_{3-\delta}$ ($x = 0.05$). Lines are drawn as guides to the eye.

state of Y^{3+} does not change, the relative atomic ratio Y/(Fe + Pd) increases when Y_2O_3 is extruded upon partial reduction of $YFe_{1-x}Pd_xO_{3-\delta}$, and decreases as Y_2O_3 and Pd are reinserted into the hexagonal structure upon reoxidation (Table 3).

In the O 1s region, two peaks are clearly resolved at 529.5 and 531.6 eV [Figure 7c]. The peak positions are unaffected by the presence of Pd^{2+}, although the peak at higher binding energy is relatively less intense for Pd-containing samples. In principle, the two signals, separated by 2.1 eV, could be assigned to the two types of lattice oxygens in the hexagonal structure. However, it has been reported that although all oxygen positions are equivalent in the garnet structure, $Y_3Al_5O_{12}$ also shows two peaks in the O 1s region.[31] The origin of the two O 1s peaks, 2.1−2.3 eV apart, in a film of perovskite $SmFeO_3$ was investigated by exposing the film to prolonged high vacuum in the XPS chamber.[32] It was found that the intensity of the peak at higher binding energy decreased gradually with increasing exposure time, while the intensity of the peak at lower binding energy remained constant, leading to the assignment of these two peaks to surface oxygen and lattice oxygen, respectively. For various oxide powders in ultra high vacuum or perovskite oxides prepared at different temperatures, the signal for surface oxygen, at 531.5 eV, disappeared gradually with increased heating or calcination temperature.[33,34] The results agree well with those reported for perovskite $LaFeO_3$, with lattice oxygen at 529.8 eV and surface oxygen at 531.7 eV.[35] Surface oxygen is likely associated with the OH-terminated surface resulted from sample preparation. Since the Pd-substituted materials were calcined at a higher temperature than the unsubstituted material, a lower surface hydroxyl content is anticipated. A decreased amount of lattice oxygen on reduction of $YFe_{1-x}Pd_xO_{3-\delta}$ ($x = 0.10$) in 5% H_2 is expected to accompany the partial reduction of Fe^{3+} to Fe^{2+} in the hexagonal structure. An increased surface hydroxyl signal in this sample, which has also been seen upon reducing several perovskites under hydrogen,[36] can be partially ascribed to the increased surface area after reduction (see the next section).

Surface Area and Morphology. Surface areas were determined by N_2 sorption measurements. Typical isotherms of as-prepared and reduced samples are shown in Figure 8a. The profiles are characteristic of mesoporous materials. Pore size distributions were modeled by the BJH method [Figure 8b]. The average pore size is around 10 nm. The maxima of the pore size distribution curves shift slightly upon Pd substitution and reduction. Pore volumes are greatly increased for reduced samples in the mesopore range of 10−20 nm. There is a slight decrease in surface area upon Pd-substitution (from 18 to 14 m^2/g), but a dramatic increase in surface area upon reduction [Figure 8c]. In fact, the surface area doubles (from 14 to 28 m^2/g) for $YFe_{1-x}Pd_xO_{3-\delta}$ sample with 10 at% Pd substitution. Porosity in the as-prepared materials is created during the drying process, when the liquid phase is removed from the gel, and the calcination thereafter with additional polycondensation. Reduction involves partial decomposition of the structure and breakdown of crystallites, which can result in enhancement of the surface area.

Scanning electron microscopy at high resolution (Figure 9) reveals some differences in the samples before and after reduction, with some porosity developing upon reduction. The increase in surface roughness and porosity after reduction is consistent with the N_2 sorption measurements. Metallic Pd nanoparticles in the reduced samples were detected by backscattered electron imaging, which is sensitive to the higher atomic number of Pd, and by transmission electron microscopy combined with EDX analysis (Figure 10). The particle sizes are mostly around 10 nm, based on TEM analysis [Figure 10c and d], consistent with the XRD analysis. Note again that TEM [Figure 10c] suggests porosity in the reduced samples.

Catalytic CO Oxidation. Catalytic oxidation of CO (1000 ppm) in excess O_2 (10%, balanced with N_2, redox stoichiometry of oxygen to CO, $S = 200$) was studied, to mimic the oxidizing conditions in the exhaust gas of lean-burn diesel engines. The activities of the as-prepared, reduced and reoxidized forms of $YFe_{1-x}Pd_xO_{3-\delta}$ were evaluated under continuous flow conditions at atmospheric pressure. The light-off profiles in Figure 11 show that Pd-substitution dramatically lowers the temperature required for 50% conversion, from 245 °C for $YFeO_3$ to 110 °C for $YFe_{1-x}Pd_xO_{3-\delta}$ ($x = 0.10$). A similar phenomenon was reported for $BaCe_{1-x}Pd_xO_{3-\delta}$.[9] The reactions reach a maximum conversion of approximately 90%. Since the as-prepared catalyst has low porosity, this is likely a result of incomplete filling of the reactor cross-section by the catalyst pellet. The reactivity is apparently unaffected by the partial reduction of Pd^{2+} to Pd^0 upon treating the as-prepared catalyst at 450 °C for 5 h, since the light-off temperature, T_{50}, remains unchanged. This suggests that oxidized Pd in the partly reduced forms of the hexagonal oxide is the active species

(31) Pawlak, D. A.; Wozniak, K.; Frukacz, Z.; Barr, T. L.; Fiorentino, D.; Seal, S. *J. Phys. Chem. B* **1999**, *103*, 1454.
(32) Aono, H.; Sato, M.; Traversa, E.; Sakamoto, M.; Sadaoka, Y. *J. Am. Ceram. Soc.* **2001**, *84*, 341.
(33) Gonzalez-Elipe, A. R.; Espinos, J. P.; Fernandez, A.; Munuera, G. *Appl. Surf. Sci.* **1990**, *45*, 103.
(34) Kaliaguine, S.; Van Neste, A.; Szabo, V.; Gallot, J. E.; Bassir, M.; Muzychuk, R. *Appl. Catal., A* **2001**, *209*, 345–358.
(35) Fierro, J. L. G.; Tejuca, L. G. *Appl. Surf. Sci.* **1987**, *27*, 453.
(36) Marcosa, J. A.; Buitragob, R. H.; Lombardo, E. A. *J. Catal.* **1987**, *105*, 95.

in the presence of the CO/O_2 mixture. At 120 °C, the activity remained constant over a period of 8 h. XPS analysis of the surface composition of $YFe_{1-x}Pd_xO_{3-\delta}$ ($x = 0.10$) postcatalysis revealed that Pd remains fully oxidized in the as-prepared and reoxidized materials (Table 3). However, for the reduced material, exposure to the lean CO/O_2 mixture during catalysis results in an increase, from 28% to 58% (after around 18 h on-stream), in the fraction of near-surface Pd^{2+} (Figure 12). It appears that only a fraction of the Pd present in the host lattice participates in forming the active phase, since the catalyst with the lower Pd loading, $YFe_{1-x}Pd_xO_{3-\delta}$ ($x = 0.05$), has similar activity ($T_{50} = 100$ °C) (Figure 13). The origin of this interesting behavior and the precise nature of the active phase are under investigation.

Conclusions

Successful preparative routes to hexagonal $YFe_{1-x}Pd_xO_{3-\delta}$ ($0 \leq x \leq 0.1$) compounds at relatively low temperatures (near 750 °C) have been developed. The previously reported ingress and egress of Pd, driven by redox in perovskite structures, was reproduced in this nonperovskite host. The low-temperature catalytic activity exhibited for CO oxidation is very encouraging and could be associated with the presence of ionic Pd^{2+} in the oxide host rather than with Pd^0 nanoparticles. This work contributes a fundamental understanding of the correlation between bulk structure, surface chemistry, and catalytic behavior of complex oxide hosts containing Pd^{2+} and suggests guidelines for the design of new catalysts with decreased amounts of platinum group metals.

Acknowledgment. This work was supported by Department of Energy (DOE) Office of Basic Energy Sciences (BES) through grant DE FG02-05ER15725. We acknowledge use of facilities of the UCSB Materials Research Laboratory, supported by the National Science Foundation (DMR05-20415). The identification of any commercial product or trade name does not imply endorsement or recommendation by the National Institute of Standards and Technology.

CM801534A